



Computational and Experimental Ice Accretions of Large Swept Wings in the Icing Research Tunnel

Gustavo E. C. Fujiwara^{*}, Michael Bragg[†], Stephanie Camello[‡], and Christopher Lum[§]

University of Washington, Seattle, WA, 98195, USA

A comparison of computational and experimental ice accretions is presented for three full-scale leading edge swept-wing models spanning from floor to ceiling in the NASA Glenn Icing Research Tunnel (IRT) at three different spanwise stations of the 65%-scale Common Research Model. Experimental ice shapes were generated on the leading edge of each model for a set of icing conditions, and then digitized with a 3D laser scanner. Computational simulations were done for the same flow and icing conditions of the experiment, utilizing CFD (OVERFLOW 3D RANS) for the flowfield solutions, and LEWICE3D for the 3D ice accretion calculations. Results showed both good ice accretion agreement and the need to further explore and better understand the complex 3D flowfield and ice accretion modeling.

Nomenclature

α	= angle of attack	η	= percent semispan
b	= reference semispan	δ_f	= model flap deflection
c	= reference chord	AR	= model aspect ratio
C_p	= pressure coefficient	h/c	= model height to chord ratio
q	= dynamic pressure	P	= pressure
LWC	= liquid water content	T	= temperature
MVD	= mean volumetric diameter	$RANS$	= Reynolds-Averaged Navier-Stokes

I. Introduction

ICE accretion and its aerodynamic effect on three-dimensional swept wings are extremely complex phenomena important to the design, certification and safe operation of small and large transport aircraft. A deeper fundamental understanding of this topic is of great interest to the aeronautical industry and the regulatory agencies, not only to ensure aviation safety, but also to satisfy the increasing demands to balance trade-offs in aircraft efficiency, cost and noise that tend to compete directly with allowable performance degradations over an increasing range of icing conditions.

In the United States, the Federal Aviation Administration (FAA) requires aircraft manufacturers to demonstrate that these aircraft can safely operate under icing conditions consistent with Appendix C of Title 14 Parts 25 and 29 in the U.S. Code of Federal Regulations (CFR). While these regulations set forth standard icing conditions for use in certification, they do not specify methods to demonstrate compliance with federal regulations. Thus, a manufacturer must work with the FAA to determine a certification plan. While some of these tests are performed in flight on the actual aircraft, flight testing a large commercial transport represents a significant cost due to the test aircraft and operations as well as the potential expense of making changes to achieve compliance late in the design process. Thus, manufacturers of larger aircraft need to test ice protection systems (IPS) and airframe's inherent ability to handle performance degradation due to ice, early in the design so that these expenses can be mitigated. Additionally, flight testing does not provide an adequately controlled matrix of test conditions for commercial aircraft certification. This results in a continued need for icing wind tunnel testing and has motivated an effort to apply computational tools to the aircraft certification process.

The use of Computational Fluid Dynamics (CFD) for icing applications started in the 1970s,^{1,2} and has played an increasingly important role in aircraft certification and ice protection systems design. However, computational methods alone are not sufficient for aircraft certification. Significant knowledge gaps remain for swept-wing geometries

^{*}Graduate Student (Ph.D.), Department of Aeronautics & Astronautics, fujiwar2@uw.edu, AIAA Student Member.

[†]Dean, College of Engineering and Professor of Aeronautics & Astronautics, mbragg@uw.edu, Fellow AIAA.

[‡]Graduate Student, Department of Aeronautics & Astronautics, scamello@uw.edu, AIAA Student Member.

[§]Research Assistant Professor, Department of Aeronautics & Astronautics, lum@u.washington.edu, Member AIAA.

and large-droplet icing conditions, and there is a lack of high-quality experimental data available in the public domain to evaluate computational simulation performance on swept wings. Thus, manufacturers rely heavily on icing wind tunnel tests to determine impingement regions, ice shapes, and to test anti-ice systems. Icing wind tunnels are used for aircraft certification to reduce costs, provide a controlled test matrix of conditions, and validate computational icing tools.

Yet, the size of aircraft models that can be tested in wind tunnels is limited by the size and capability of existing facilities. Large wings, such as those found on modern narrow and wide-body commercial transports, cannot fit in existing test sections without being dramatically scaled. One way to circumvent this problem is to geometrically scale down the entire geometry to fit inside the tunnel test section and then scale the icing conditions (MVD, LWC, speed, etc) to obtain icing similitude, as described by Anderson.³ Another method relies on designing a wing model with the full-scale leading edge of the wing and a redesigned shortened aft section that produces similar ice accretion characteristics around the leading edge, such that the need for scaling the icing conditions can be reduced or eliminated. This type of model is referred to as a hybrid,^{2,4} and was be the kind of model studied in this paper.

The current work is part of a larger collaborative research program on Swept-Wing Icing Aerodynamics, involving NASA, the FAA, the Office National d'Etudes et de Recherches Aérospatiales (ONERA), the Boeing Company, the University of Washington, the University of Illinois at Urbana-Champaign (UIUC), and the University of Virginia. This overall research effort is described in detail by Broeren et al.⁵ This paper falls under Phases III and VII of this larger effort. The objective of Phase III is to better understand how ice shapes on a large-scale, swept-wing can be replicated in existing icing tunnels using a hybrid model, and identify key indicators in flowfields that result in successful representation of full-scale icing. The objective of Phase VII is to assess the ability of Computational Fluid Dynamics (CFD) coupled with icing physics computational simulations to accurately model ice accretion in this environment.

This paper presents a comparison of the experimental data collected during the Phase III tests in the IRT with the Phase VII computational predictions utilizing OVERFLOW for the 3D flow solution and LEWICE3D for the 3D droplet trajectory and ice accretion computations.

II. Aircraft and Model Geometries

The 65%-scale Common Research Model,⁶ referred to as CRM65, was selected as the reference aircraft baseline wing for this research. The CRM65 has a semispan of $b/2 = 751.89$ in. (19.10 m), an aspect ratio of $AR = 9.0$, a taper ratio of 0.275, and a leading-edge sweep angle of 37.15 deg., making it comparable in size to existing narrow-body commercial transports, such as the B757-200. It was determined that the full configuration of the CRM65 was not necessary for the objectives of this research. Therefore, the work performed was done on the wing-body only (WB) configuration.

After selecting the baseline aircraft configuration, a set of generic icing mission scenarios were identified to determine the critical ice shapes for a typical large transport aircraft. These scenarios were called the baseline icing conditions and consisted of six aerodynamic cases and seventeen icing conditions.⁷⁻⁹ The aerodynamic solutions of the CRM65 aircraft in free air at flight speed were obtained with the 3D RANS solver OVERFLOW,¹⁰ and then used to generate the ice accretion simulations with LEWICE3D. The set of aerodynamic solutions was called Clean Flight Baseline (CFB), and the set of ice accretion simulations called Iced Flight Baseline (IFB).

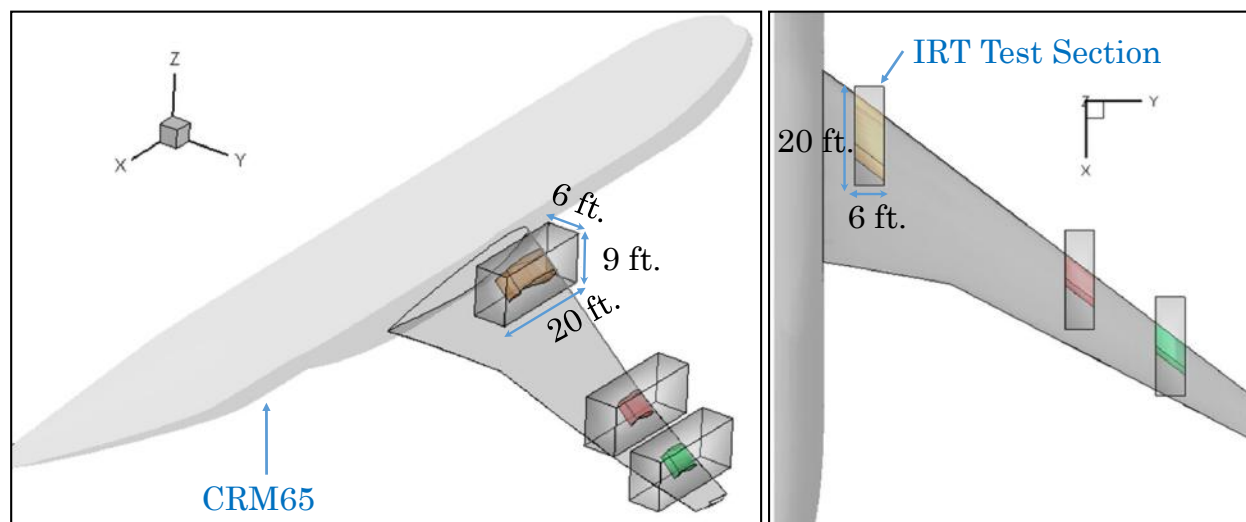

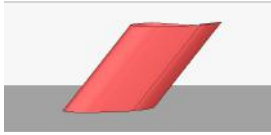



Figure 1: CRM65 aircraft geometry in comparison to IRT wing models and test section dimensions.⁷

Once the baseline CFD and icing analyses were performed for the selected wing geometry, the specific spanwise stations for the hybrid model designs were selected. The goal was to identify the minimum number of locations along the wing that could represent the ice accretion along the entire swept wing.^{2,4,7-9} Three stations were selected at 20%, 64%, and 83% semispan position of the CRM65, and hybrid wing models were designed for each of these stations applying the method developed by Fujiwara et al.^{2,4,7}

Figure 1 displays the three designed hybrid models inside the IRT test section (6 ft x 9 ft x 20 ft) in comparison to the reference aircraft geometry of the CRM65, illustrating the challenge of full-scale testing a large swept wing model in existing icing wind tunnels. Both oblique and top views are displayed to scale. The geometric characteristics of the three designed hybrid wing models are shown in Table 1. For airfoil and flap coordinates refer to Fujiwara.⁷

Table 1: Inboard, Midspan, and Outboard model geometric characteristics

	IB	MS	OB
Model Name	Inboard	Midspan	Outboard
CRM65 Spanwise Station, η	20%	64%	83%
Scale Factor, $SF = \frac{Chord_{CRM65}}{Chord_{IRT Model}}$	2.25	2	1.5
Model streamwise chord	161.8 in (13.48 ft)	74.6 in (6.22 ft)	74.0 in (6.17 ft)
Aspect Ratio, AR	0.45	0.96	0.97
Height to Chord Ratio, h/c	0.67	1.45	1.46
Thickness	19.2 in	9.2 in	8.2 in
Models			

Flaps: • Modified NACA6412 with rounded leading edge for more constant gap/overlap over range of flap deflections

• 1/4 of total chord (main element + flap)

• 1.5% gap / 1.5% overlap of total chord

III. Experimental Data

The NASA Glenn Icing Research Tunnel (IRT) is a closed-return, atmospheric, refrigerated wind tunnel, capable of reaching calibrated speeds between 50 and 325 knots (empty), and producing calibrated supercooled water droplets between 15 - 270 μm with static temperatures ranging from -40 to 20 °C. See Steen et al.,¹¹ Soeder et al.¹² for details.

Three wind tunnel campaigns took place at the IRT between March-May and Sept-Oct. of 2015 to test the IB, MS, and OB hybrid models. A subset of common conditions established across the test matrices for the three models was chosen to be reproduced with computational tools, for comparison. These six test conditions for the IB, MS, and OB hybrid models had the same nominal values, except for the flap deflections. The actual measured values in the tunnel are presented in Tables 2 - 4, for completeness. For additional information, please refer to Broeren et al.¹³

Table 2: Inboard Model Icing Conditions Tested

Run ID (Nickname)	Run No.	α	Flap	Speed	P_{total}	P_{static}	T_{total}	T_{static}	MVD	LWC	Time	Mach	q	Re
		Deg.	Deg.	Knots	psia	psia	Deg.C	Deg.C	m	g/m ³	min		psf	
3 ("Venetian Blind")	TG2421	3.7	13.8	129	14.35	13.94	-3.9	-6.1	25.0	1.00	29	0.20	58.12	20.36x10 ⁶
4 ("Maximum Scallop")	TG2411	3.7	13.7	129	14.62	14.20	-6.4	-8.6	25.0	1.00	29	0.20	59.57	21.05x10 ⁶
5 ("Small Gap")	TG2402	3.7	13.6	130	14.31	13.90	-8.8	-11.0	25.0	1.00	29	0.21	59.11	21.00x10 ⁶
6 ("Incomplete Scallop")	TG2426	3.7	13.8	129	14.49	14.06	-11.3	-13.5	25.0	1.00	29	0.21	60.30	21.60x10 ⁶
9 ("Streamwise/Rime")	TG2406	3.7	13.8	130	14.40	13.96	-18.0	-20.3	25.0	0.60	23	0.21	61.55	22.50x10 ⁶
23 ("WB33 Direct App. C")	TG2424	3.7	13.8	128	14.55	14.14	-3.2	-5.4	28.0	0.91	45	0.20	57.82	20.37x10 ⁶

Table 3: Midspan Model Icing Conditions Tested

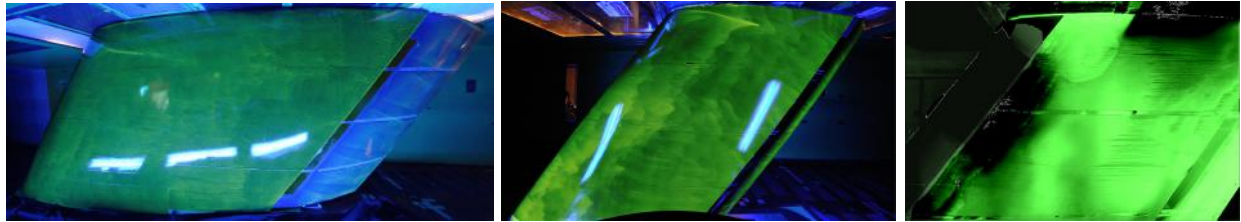
Run ID (Nickname)	Run No.	α	Flap	Speed	P_{total}	P_{static}	T_{total}	T_{static}	MVD	LWC	Time	Mach	q	Re
		Deg.	Deg.	Knots	psia	psia	Deg.C	Deg.C	m	g/m ³	min		psf	
3 ("Venetian Blind")	TH2438	3.7	24.9	129	14.38	13.97	-4.0	-6.2	25.0	1.00	29	0.20	57.94	9.39x10 ⁶
4 ("Maximum Scallop")	TH2452	3.7	24.9	129	14.14	13.74	-6.4	-8.6	25.0	1.00	29	0.20	57.41	9.38x10 ⁶
5 ("Small Gap")	TH2458	3.7	24.9	130	14.23	13.81	-8.8	-11.0	25.0	1.00	29	0.21	58.91	9.64x10 ⁶
6 ("Incomplete Scallop")	TH2432	3.7	25.0	130	14.46	14.03	-11.4	-13.6	25.0	0.99	29	0.21	60.64	9.99x10 ⁶
9 ("Streamwise/Rime")	TH2439	3.7	25.1	130	14.37	13.93	-18.1	-20.3	25.0	0.60	23	0.21	61.61	10.38x10 ⁶
23 ("WB33 Direct App. C")	TH2514	3.7	24.8	129	14.43	14.02	-3.2	-5.4	27.6	0.91	45	0.20	57.67	9.35x10 ⁶

Table 4: Outboard Model Icing Conditions Tested

Run ID (Nickname)	Run No.	α Deg.	Flap Deg.	Speed Knots	P_{total} psia	P_{static} psia	T_{total} Deg.C	T_{static} Deg.C	MVD m	LWC g/m ³	Time min	Mach	q psf	Re
3 ("Venetian Blind")	TI2462	3.7	14.0	129	14.37	13.96	-3.9	-6.1	25.2	1.00	29	0.20	58.17	9.33x10 ⁶
4 ("Maximum Scallop")	TI2461	3.7	14.1	130	14.38	13.96	-6.4	-8.7	25.2	0.99	29	0.21	59.46	9.55x10 ⁶
5 ("Small Gap")	TI2488	3.7	13.9	130	14.42	14.00	-8.8	-11.1	25.2	0.99	29	0.21	60.03	9.72x10 ⁶
6 ("Incomplete Scallop")	TI2492	3.7	14.1	130	14.34	13.91	-11.3	-13.6	25.2	0.99	29	0.21	60.13	9.82x10 ⁶
9 ("Streamwise/Rime")	TI2484	3.7	14.1	130	14.35	13.91	-18.1	-20.3	24.8	0.60	23	0.21	61.93	9.31x10 ⁶
23 ("WB33 Direct App. C")	TI2468	3.7	14.0	130	14.32	13.91	-3.2	-5.4	27.6	0.91	45	0.20	57.91	9.26x10 ⁶

Before the icing runs, some dry runs were performed to do the aerodynamic calibration of the model. This process consisted of varying angle of attack for different flap settings, to find out what angles of attack and flap deflections would achieve the target attachment line locations on the centerline of the models for the corresponding test conditions. This was done in real time by processing the pressure data measured in a streamwise row of pressure taps along the centerline of each model.

Additional runs were done utilizing flow visualization techniques such as fluorescent oil, in which oil particles are roller painted onto the model surface, the wind is turned on briefly, and ultraviolet light is used to visualize flow features and surface streamlines, as shown for the Inboard and Midspan models in Fig. 2a and 2b, respectively. No fluorescent oil run was done for the Outboard model, but surface streamlines can be seen after a short icing run for which the droplets ran back and refroze on the model surface, Fig. 2c, after adjusting the image contrast and color to green. For more detailed images and procedural description, the reader is encouraged to check Broeren et al.¹³



(a) Inboard model.

(b) Midspan model.

(c) Outboard model.

Figure 2: Experimental flow visualization of models inside IRT.

After the aerodynamic calibration, the instrumented leading edge that contained the pressure taps was replaced by a non-instrumented leading edge where the ice accretions would form. For each icing run, the tunnel was set at the test conditions until both target speed and temperatures settled. Only then, the droplets spray was turned on.

At the end of each icing run, the ice shapes were painted with special paint to increase reflectivity, and then digitized with a 3D laser scanner, as described by Lee et al.^{14,15} Each of these digitized scans consisted of a point cloud that were later post-processed to form a continuous surface geometry.¹⁵ Once processed, these ice shapes CAD geometries were manipulated to extract 2D cuts normal to the leading edge of the model, similar to taking ice tracings.¹⁴

This process of extracting 2D cuts out of the digitized ice shape is shown in Fig. 3, where 30 normal cuts perpendicular to the model leading edge, 0.2 inch apart, were extracted and plotted in 2 dimensions. Then the outer boundary that leads to the Maximum Combined Cross Section (MCCS) of the ice sections was obtained for later comparison to the computational simulations, giving a conservative (large) shape that was deemed closest to hand tracing.

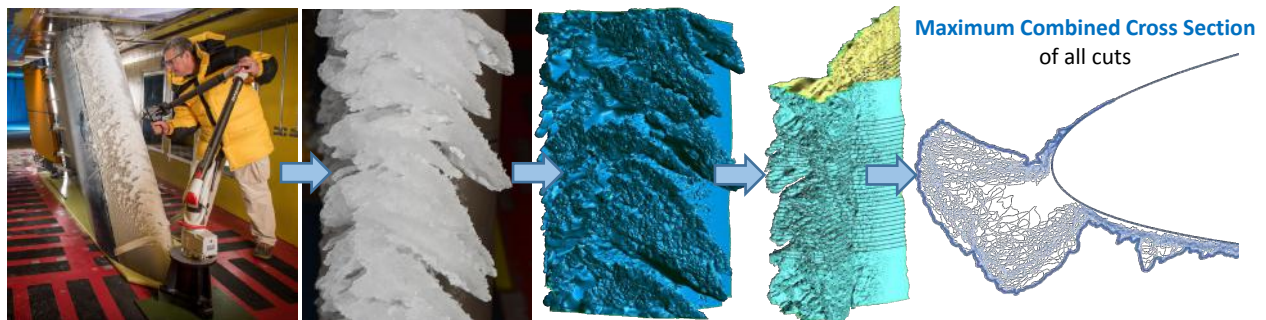


Figure 3: Extraction of 2D cuts from digitized scan of experimental ice shape.

IV. Computational Simulations

The same conditions presented in Tables 2-4 for the experiments were reproduced with computational tools, utilizing OVERFLOW for the flow solutions and LEWICE3D¹⁶ for the ice accretion calculations.

CFD: 3D RANS (OVERFLOW)

The 3D RANS simulations utilizing OVERFLOW with $k - \omega$ ¹⁷ turbulence model were conducted by Boeing, for the same geometries tested in the tunnel, with the absence of the model floor plate for meshing simplicity.

Notice how all the six different icing conditions corresponded to the same model angle of attack and flap deflection, and shared the same tunnel speed for the three models. This required the generation of only one aerodynamic CFD flowfield solution per model. These solutions are presented in Fig. 4, where the upper surface pressure coefficient contours and surface streamlines are shown for each of the models at $\alpha = 3.7^\circ$ and approximately 130 knots. The flap deflection of each model was kept the same as that required in the experiment to reach its target attachment line location.

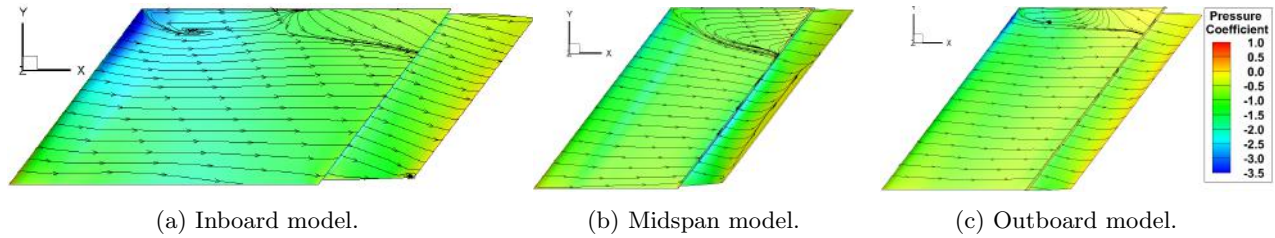


Figure 4: Models upper surface pressure coefficient contours and surface streamlines from OVERFLOW.

Fig. 5 presents the pressure coefficient comparison between the experiment and the computational simulations for three streamwise stations at $Y = 18, 36$ (centerline), 54 inches from the IRT floor. Recall the IRT floor is at $Y = 0$ and the ceiling at $Y = 72$ inches. Overall, the OVERFLOW simulations matched the experimental data for all three models, with a slight under prediction of the suction peak magnitude by the computational simulations.

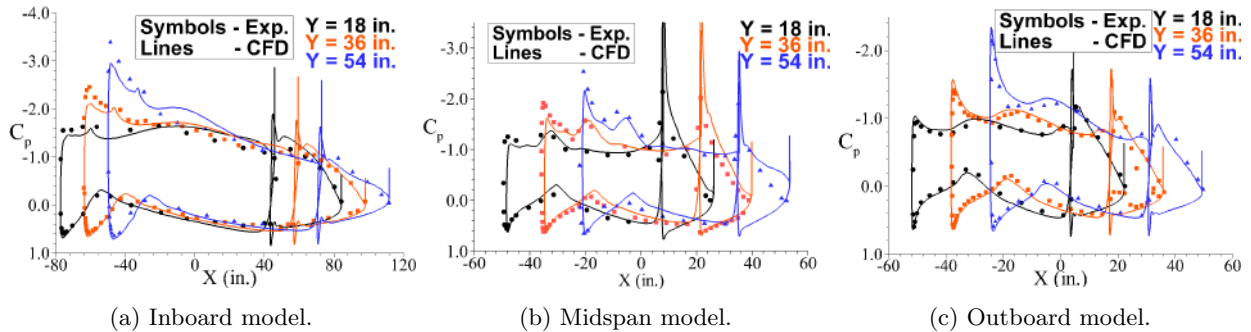


Figure 5: Models pressure coefficient comparison between IRT and OVERFLOW.

Figure 6 shows the zoomed region of the centerline cut ($Y = 36$ inches) pressure coefficient as a function of the wrap distance (positive values on lower surface) from the highlight (forward most point of the model when at zero angle of attack). The close match of the CFD simulations to the experimental attachment line locations was the main parameter to match the ice accretions, as shown is previous studies.^{2,7-9} For more details, see Broeren et al.¹³

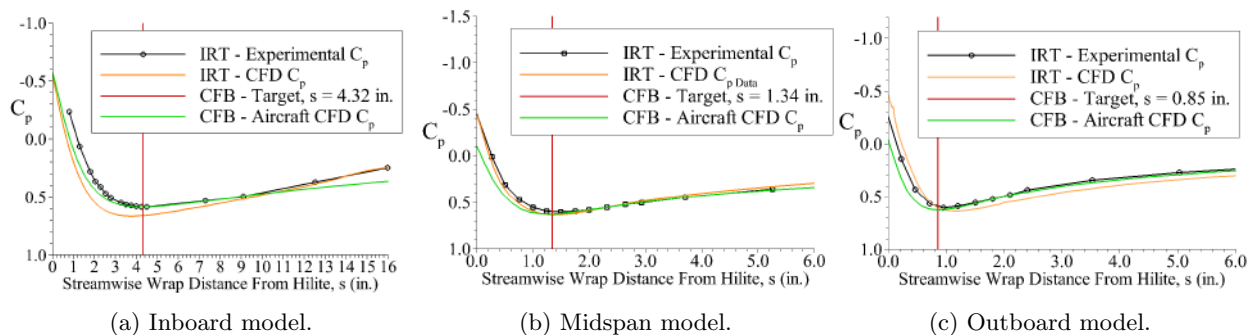
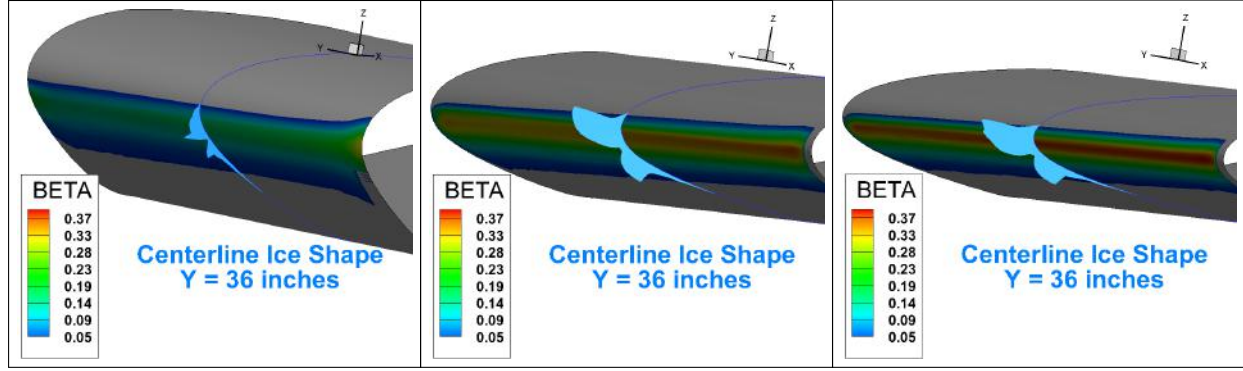


Figure 6: Models attachment line location comparison between IRT, OVERFLOW, and CFB (target).

ICE ACCRETION: LEWICE3D

The CFD solutions for each of the three models was then used to generate the LEWICE3D ice accretions with the parallel version of the code, called TRAJMC3D (version 2.48), for the conditions corresponding to the cases from Tables 2 - 4. The code utilizes the user-supplied 3D flow solution on a structured or unstructured grid to calculate the Lagrangian droplet trajectories and compute the single time step ice accretions along user-defined 3D strips on the model. For the present work, only the centerline perpendicular cut ice shape was calculated for each case. The 10-bin IRT droplet size distribution was used in LEWICE3D, based on values measured by Papadakis et al.¹⁸

An example of the resulting centerline ice shape ($Y = 36$ inches, perpendicular to the leading edge), and corresponding collection efficiency contours (beta) for Run ID 3 ("Venetian Blind") case is presented in Fig. 7.



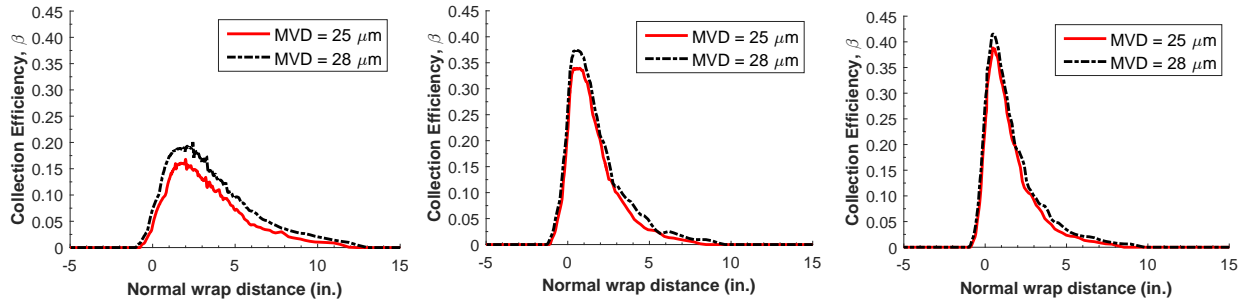
(a) Inboard model run TG2421.

(b) Midspan model run TH2438.

(c) Outboard model run TI2462.

Figure 7: LEWICE3D ice shape and collection efficiency (beta) of models for RunID 3 ("Venetian Blind").

Figure 8 displays the collection efficiencies as functions of the centerline normal wrap distance, for all three models and two conditions. Positive values of s are on the lower surface. The first condition corresponds to Run ID 3, 4, 5, 6, and 9, which have the same particle size ($MVD = 25 \mu m$), while the second condition corresponds to Run ID 23 with $MVD = 28 \mu m$, both utilizing the 10-bin IRT droplet distribution.¹⁸ Comparing the different models one can notice how the thinner models produced higher collection efficiency. Comparing the two MVD values, the larger droplets tend to impact over a larger portion of the leading edge and have slightly higher peak, β_{max} .



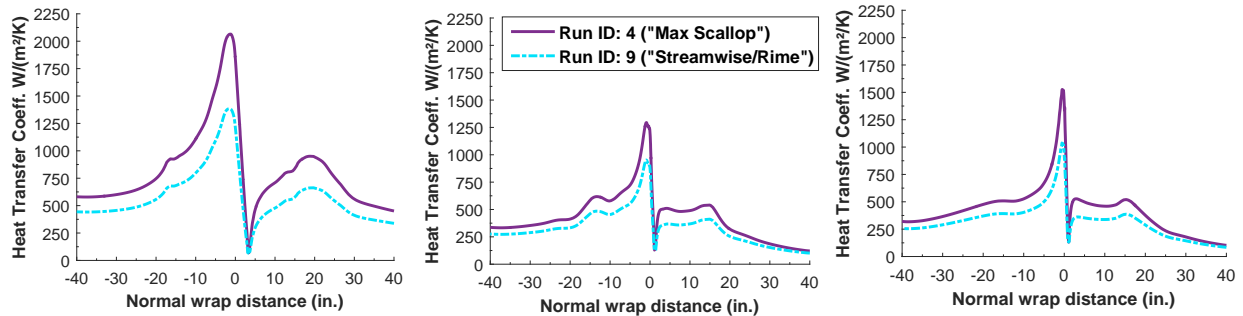
(a) Inboard model.

(b) Midspan model.

(c) Outboard model.

Figure 8: LEWICE3D centerline collection efficiencies (beta) for Run ID: 3, 4, 5, 6, 9 and Run ID: 23.

Figure 9 presents the heat transfer coefficients (HTC) as functions of the centerline normal wrap distance for all three models and two conditions. Notice how the Inboard model HTC values are higher than the other models.



(a) Inboard model.

(b) Midspan model.

(c) Outboard model.

Figure 9: LEWICE3D centerline heat transfer coefficient for Run ID: 4 and 9.

The HTC values are obtained from correlations that are function of the surface velocity on the model and the leading edge radius which determines the roughness correlation.

Finally, the freezing fractions are calculated utilizing the HTC values, and are presented in Fig. 10 as function of the normal wrap distance. Notice how the colder temperature for the Run ID 9 case yields a freezing fraction of 1 along the entire impinging region, causing particles to freeze upon impingement and making it less dependent on the HTC model correlations.

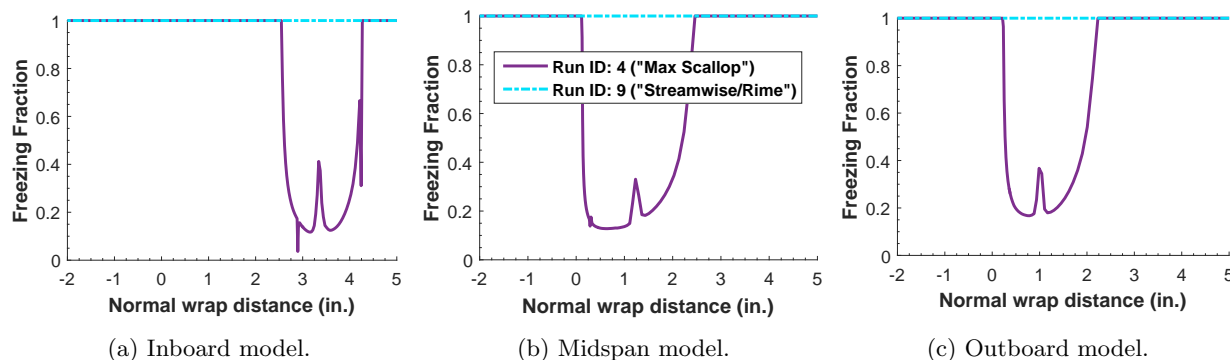


Figure 10: LEWICE3D centerline freezing fractions for Run ID: 4 and 9.

V. Ice Accretion Comparison

After extracting the 2D normal cuts of the digitized experimental ice accretions of the hybrid models at the IRT centerline, and running the CFD and LEWICE3D simulations for the same conditions, it is possible to compare the ice shapes in a two-dimensional plot.

Because scallop ice shapes are very three-dimensional, obtaining meaningful comparisons of the experimental ice shapes from the 3D scans with the LEWICE3D ice shapes can be very challenging. While the 3D scans of the scallop ice shapes present significant details and variation along the span due to the gaps between peaks, LEWICE3D is essentially a 3D droplet trajectory code with a 2D strip approach for the ice accretion calculation, so the computational ice shapes produce the overall 2D ice shape, lacking roughness and three-dimensional features.

An example of a scallop ice shape digitized and transformed into a CAD model and its corresponding LEWICE3D generated ice shape extruded along the same span is shown in Fig. 11, to illustrate the challenges of such comparison.

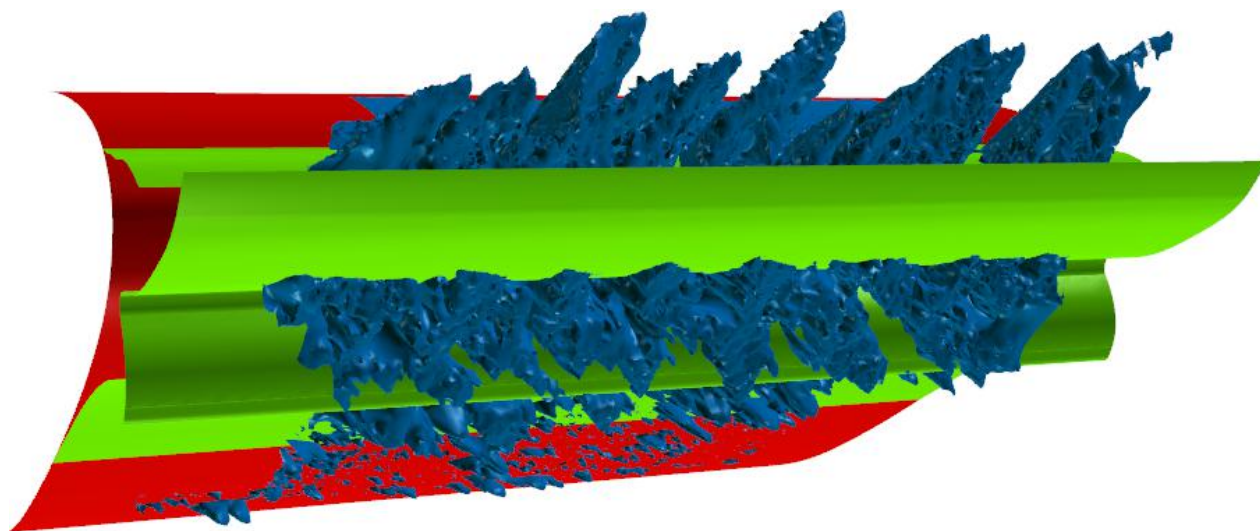


Figure 11: TH2452: IRT 3D scan (blue), LEWICE3D extruded ice shape (green), clean leading edge (red).

The comparison of the 6 icing conditions for each of the three models, as detailed in Tables 2 - 4 are presented in Fig. 12 - 17, displaying 2D plots of the Maximum Combined Cross Section (MCCS) shapes from the 3D scans and the LEWICE3D ice shapes generated for the centerline cut of the IRT models. Pictures of the actual experimental ice accretions are also displayed for perspective, above each case.

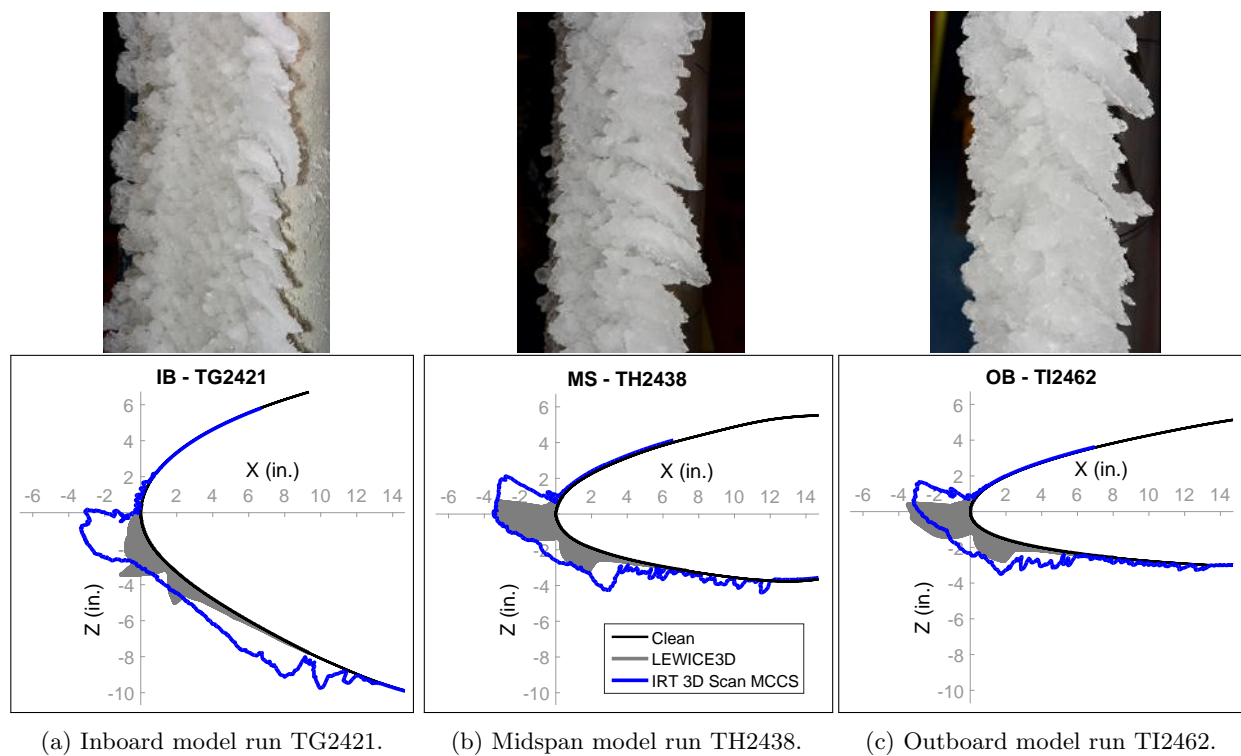


Figure 12: Run ID 3 ice condition ("Venetian Blind"). LEWICE3D ice density = 450 kg/m^3 .

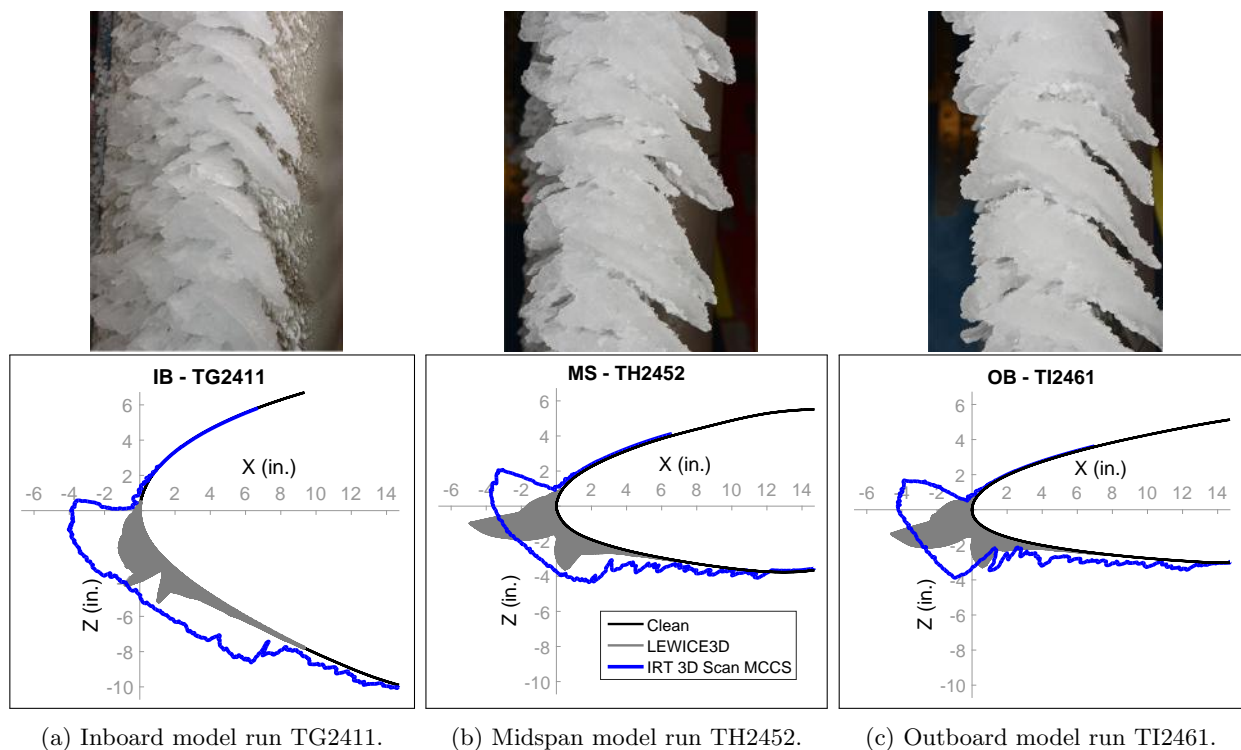


Figure 13: Run ID 4 ice condition ("Maximum Scallop"). LEWICE3D ice density = 350 kg/m^3 .

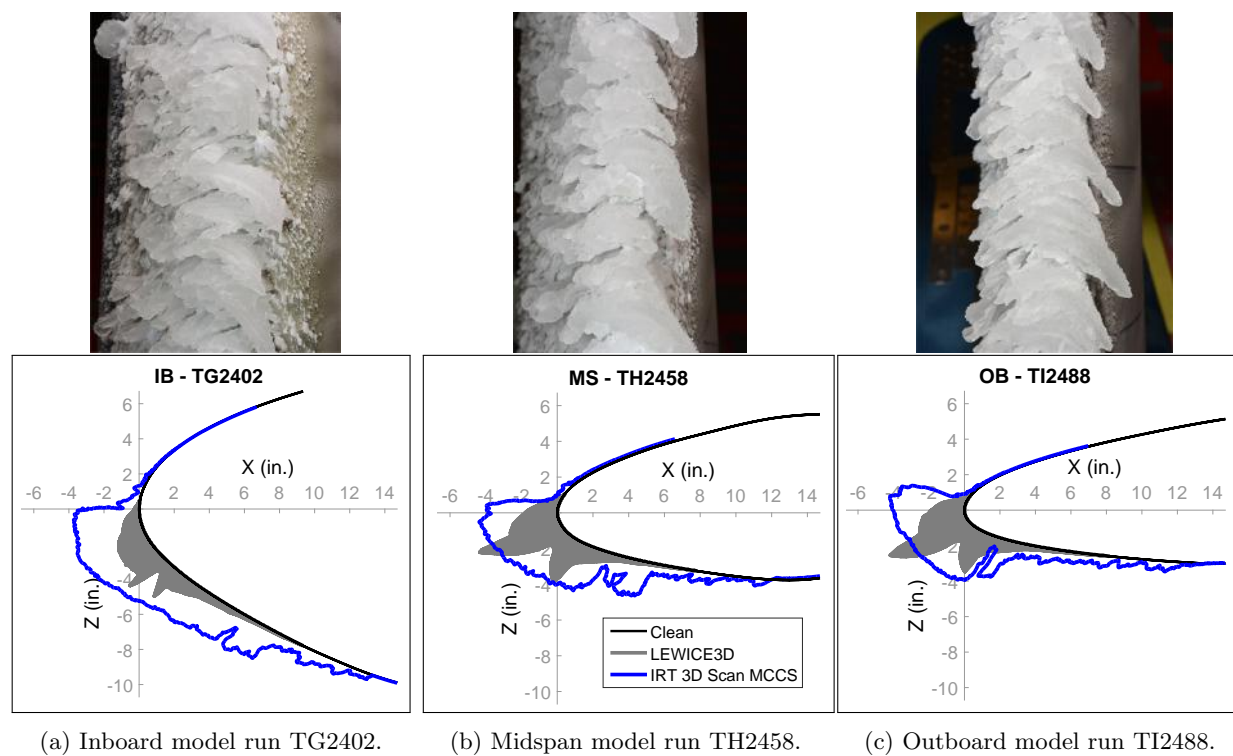


Figure 14: Run ID 5 ice condition ("Small Gap"). LEWICE3D ice density = 350 kg/m^3 .

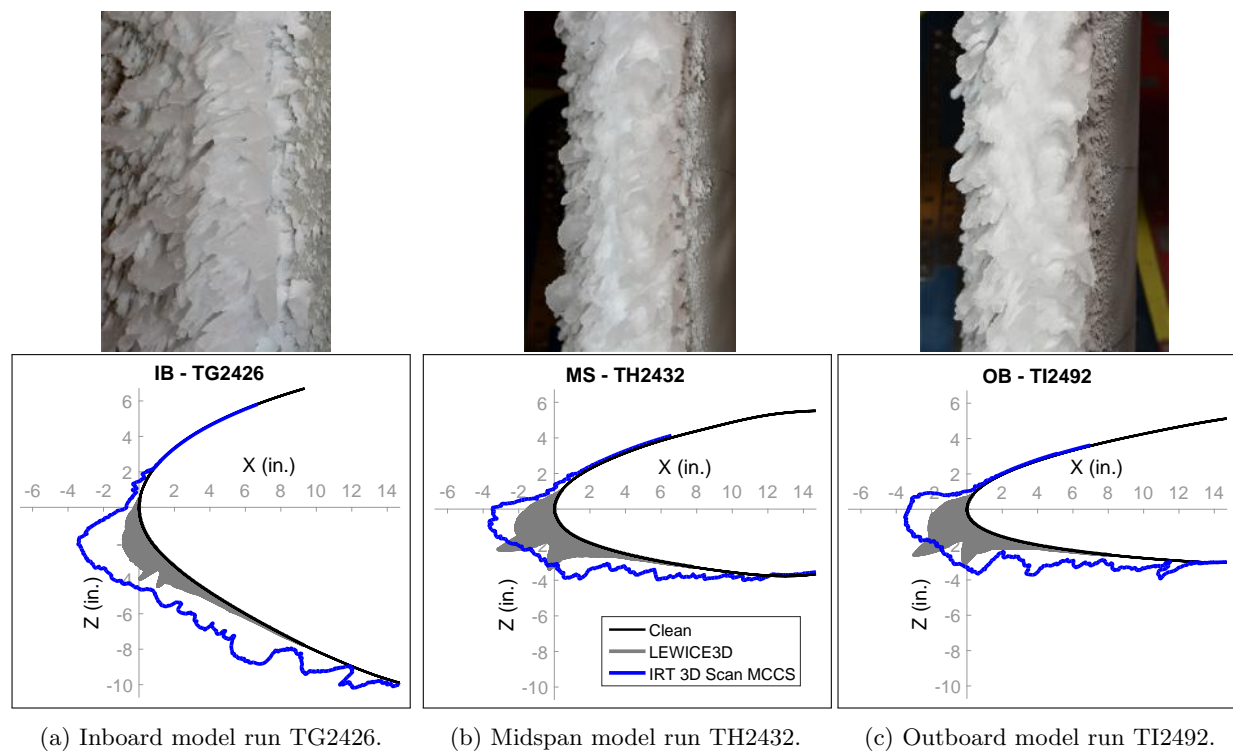


Figure 15: Run ID 6 ice condition ("Incomplete Scallop"). LEWICE3D ice density = 450 kg/m^3 .

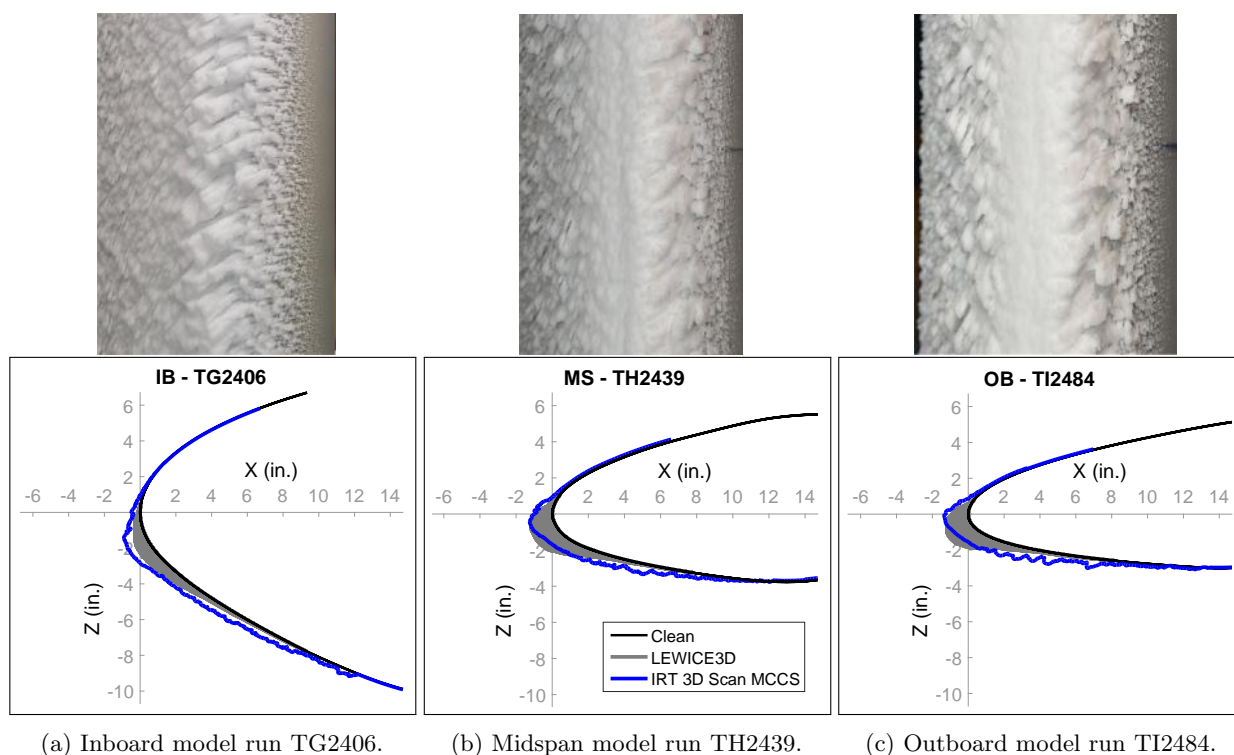


Figure 16: Run ID 9 ice condition ("Streamwise/Rime") ice condition. LEWICE3D ice density = 450 kg/m^3 .

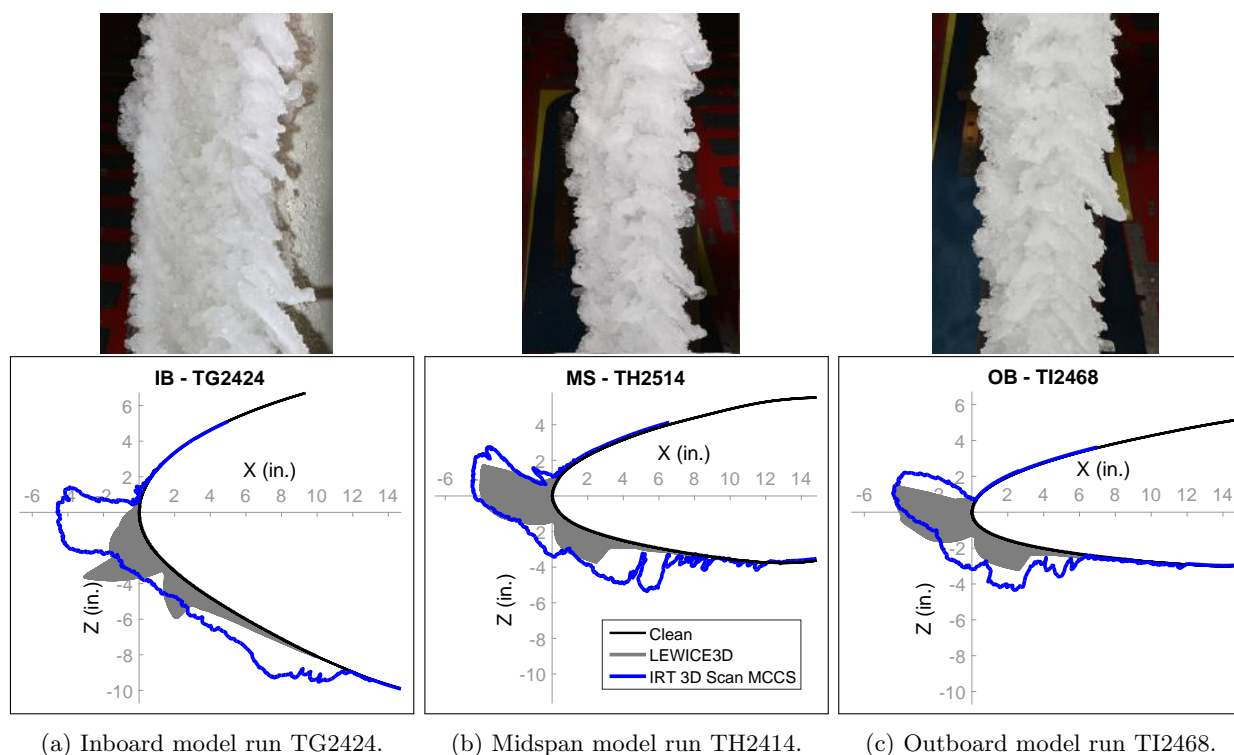


Figure 17: Run ID 23 ice condition ("WB33 Direct Appendix C"). LEWICE3D ice density = 450 kg/m^3 .

Overall, good agreement was observed between the computational simulations and the experimental data for most cases analyzed. Two of the main geometric ice shape parameters used to judge the comparison were the ice shape horn length and angle.

Among the three models, the Inboard model presented the poorest agreement between computational and experimental data. This was evidenced by the shorter accretion limits and smaller ice shape horn lengths predicted by the computational tools in comparison to the experiment. One of the possible explanations for such differences may be attributed to the lack of experimental data on very large swept wings such as the Inboard model to calibrate the computational models and correlations for heat transfer and roughness, which tend to get increasingly more important the warmer the temperatures are. The significantly larger thickness of the Inboard model compared to the other two models might have also caused larger wind tunnel blockage effects that would be hard to capture with the CFD boundary conditions specified.

The Midspan and Outboard models, on the other hand, had much closer agreement between computational predictions and experiment, specially for Run ID 3 ("Venetian Blind") and Run ID 23 ("WB33 Direct Appendix C") ice conditions, for which the ice horn length, the ice horn angle, and the ice accretion limits showed excellent agreement.

In general, the best match occurred for Run ID 9 ("Streamwise/Rime") ice condition, where the very low temperatures caused droplets to freeze almost instantly after impact, making the match less dependent on the heat transfer coefficient calculation. This served as a good control case to check if the computational predictions captured the appropriate droplet trajectory impact locations and produced the correct size of the ice accretions compared to that of the experiment.

Matching the computational horn-type ice shape predictions with the experiment, which occurs when the temperatures are closer to the freezing temperature, proved to be a more challenging task, exposing the need for improved physics models in the computational ice accretion tools. Note that while LEWICE3D's standard ice density value is 917 kg/m^3 , each computational simulation used a particular ice density value to match the experiment. Bidwell¹⁹ implemented an automatic ice density calculation in a more recent version of LEWICE3D (v 3.48) with a void density model that accounted for different leading-edge sweep angles and temperatures, on two different NACA0012 swept wings. The study used the experimental data obtained from icing runs on the swept wings in the IRT to calibrate the computational void density model, and showed tunnel measured ice densities varying between $300\text{--}450 \text{ kg/m}^3$ for the 45° -swept wing, and $350\text{--}500 \text{ kg/m}^3$ for the 30° -swept wing for static temperatures ranging from -18 to -5°C . Unfortunately, such automatic calculation feature was not available in the version of the code used for the simulations presented here, so each simulation case had the ice density values manually chosen. All the values used in the simulations were in the range between $350\text{--}450 \text{ kg/m}^3$, which were very similar to the ones measured by Bidwell.¹⁹

An important note is that the computational shapes predicted by LEWICE3D with the 3D RANS CFD simulations only capture the main 2D features of the ice shapes such as the overall contour, but not the small 2D features/details nor the spanwise variation of the very three-dimensional experimental ice shapes, specially the scallop cases. The three-dimensional characteristics of the experimental ice shapes could not be depicted in the 2D plots, but can be seen in the photographs that accompanied each 2D plot comparison. A recent investigation that showed preliminary results of an approach to predict three-dimensional ice accretion features such as ice feathers and ice scallops that resemble lobster tails is presented by Szilder et al.²⁰ The so called "morphogenetic" approach described in their work utilizes a discrete formulation in the ice accretion process that yields the ability to simulate rough and discontinuous ice structures, as opposed to traditional continuous models for a swept-wing configuration. The distributions of collection efficiency and direction of drop impingement are computed for a clean wing and they are kept constant during the ice growth simulation, similarly to what is done in LEWICE3D (called one-shot method, when there is no aerodynamic feedback from the ice that builds up on the model surface to update the flowfield). The main difference lies in the ice accretion part of the code, which uses discrete fluid elements that can lead to growth enhancement of the asperities and a shadowing effect (limited growth) for areas located behind local ice roughness elements.

VI. Conclusions

Three successful IRT icing wind tunnel campaigns were conducted for three different swept wing hybrid models that produced full-scale experimental ice accretions, representing three different stations of the CRM65 aircraft. All the ice accretion data were documented and digitized through 3D ice scans for a range of different icing conditions, as well as model pressure data and flow visualization images.

Computational simulations of the same conditions as the experiment were performed, utilizing the 3D RANS flow solver OVERFLOW and the 3D droplet trajectories calculation and ice accretion prediction software LEWICE3D. Results showed good agreement of the ice accretions between the computational simulations and the Maximum Combined Cross Section shape of the experiment in terms of geometric parameters such as the ice horn length, the ice horn angle, and the ice accretion limits. The ice densities found to provide the best fit with the experimental data agreed well with the values observed by previous experiments to calibrate the code.

The experimental swept-wing ice shapes showed all the small 2D details and features such as the roughness on top of the mean shape, as well as the 3D variations in the spanwise directions such as gaps and peaks observed for the ice scallop cases. The computational ice accretions predicted by LEWICE3D, on the other hand, were only capable of producing the smooth 2D contours of the ice shape for discrete perpendicular cuts of the wing. This comparison

highlighted the major differences in the computational and experimental ice accretions from a purely geometric perspective, emphasizing the limitation of using an essentially 2D ice accretion code to describe the formation of scallops. Whether or not these geometric feature differences also produce differences in the aerodynamic performance of these ice shapes for swept wings will be determined in future aerodynamic experiments. In any case, current strides in the direction of expanding ice accretion code capabilities to predict three-dimensional ice features are already underway.

Overall, the work presented in this paper along with the other papers from this research collaboration represent an important contribution to fill the gap for public domain swept-wing ice accretion data. A better understanding of swept wing icing aerodynamics and improved icing physics modeling of the computational tools are sought as future steps of this project.

Acknowledgments

The authors would like to thank NASA for funding for this research, under grant NNX12AB04A. Thanks to Andy Broeren, Colin Bidwell, Mark Potapczuk, Sam Lee, and the rest of the NASA Glenn Icing Research Branch for their many technical contributions, and Colin Chen, a student in the NASA Icing Branch affiliated with Universities Space Research Association, who generated the Maximum Combined Cross Sections in support of this paper. The authors also wish to thank Bernard Paul, Adam Malone, Yoram Yadlin, Toni Sclafani, and Ryan Polito from Boeing. This work was facilitated through the use of advanced computational, storage, and networking infrastructure provided by the Hyak supercomputer system at the University of Washington.

References

- ¹Bragg, M. B., Broeren, A. P., and Blumenthal, L. A., "Iced-airfoil aerodynamics," *Progress in Aerospace Sciences*, Vol. 41, No. 5, 2005, pp. 323–362.
- ²Fujiwara, G. E. C., Woodard, B. S., Wiberg, B. D., Mortonson, A. J., and Bragg, M. B., "A Hybrid Airfoil Design Method for Icing Wind Tunnel Tests," *AIAA Paper 2013-2826*, San Diego, CA, June 2013.
- ³Anderson, D. N., "Manual of scaling methods," *NASA/CR-2014-212875*.
- ⁴Fujiwara, G. E. C., Wiberg, B. D., Woodard, B., and Bragg, M. B., "3D Swept Hybrid Wing Design Method for Icing Wind Tunnel Tests," *AIAA Paper 2014-2616*, Atlanta, GA, June 2014.
- ⁵Broeren, A. P., Potapczuk, M. G., Riley, J. T., Villedieu, P., Moëns, F., and Bragg, M. B., "Swept-Wing Ice Accretion Characterization and Aerodynamics," *AIAA Paper 2013-2824*, also *NASA TM-2013-216555*, Sept. 2013.
- ⁶Vassberg, J. C., DeHaan, M. A., Rivers, S. M., and Wahls, R. A., "Development of a common research model for applied CFD validation studies," *AIAA paper 6919*, Aug. 2008.
- ⁷Fujiwara, G. E. C., "Design of 3D Swept Wing Hybrid Models for Icing Wind Tunnel Tests," *M.S. Thesis, Dept. of Aerospace Eng., Univ. of Illinois, Urbana, IL*, 2015.
- ⁸Wiberg, B., "Large-scale swept-wing ice accretion modeling in the NASA Glenn Icing Research Tunnel using LEWICE3D," *M.S. Thesis, Dept. of Aerospace Eng., Univ. of Illinois, Urbana, IL*, 2014.
- ⁹Wiberg, B., Fujiwara, G. E. C., Woodard, B., and Bragg, M., "Large-Scale Swept-Wing Icing Simulations in the NASA Glenn Icing Research Tunnel Using LEWICE3D," *AIAA Paper 2014-2617*, Atlanta, GA, June 2014.
- ¹⁰Sclafani, A. J., DeHaan, M. A., Vassberg, J. C., Rumsey, C. L., and Pulliam, T. H., "Drag Prediction for the Common Research Model Using CFL3D and OVERFLOW," *Journal of Aircraft*, Vol. 51, No. 4, 2014, pp. 1101–1117.
- ¹¹Steen, L. E., Ide, R. F., Van Zante, J. F., and Acosta, W. J., "NASA Glenn Icing Research Tunnel: 2014 and 2015 Cloud Calibration Procedures and Results," *NASA TM-2015-218758*, May, 2015.
- ¹²Soeder, R. H., Sheldon, D., Ide, R., Spera, D., and Andracchio, C., "NASA Glenn Icing Research Tunnel User Manual," *NASA TM-2003-212004*, Sept. 2003.
- ¹³Broeren, A. P., Potapczuk, M. G., Lee, S., Malone, A. M., Paul, B. P., and Woodard, B. S., "Ice-Accretion Test Results for Three Large-Scale Swept-Wing Models in the NASA Icing Research Tunnel," *AIAA 8th Atmospheric and Space Environments Conference, Washington D.C., June 13–17, 2016 (submitted for publication)*, 2016.
- ¹⁴Lee, S., Broeren, A. P., Addy Jr, H. E., Sills, R., and Pifer, E. M., "Development of 3-D Ice Accretion Measurement Method," *AIAA Paper 2012-2938*, June 2012, also *NASA TM-2012-217702*, Sept. 2012.
- ¹⁵Lee, S., Broeren, A. P., Kreeger, R. E., Potapczuk, M., and Utt, L., "Implementation and Validation of 3-D Ice Accretion Measurement Methodology," *AIAA Paper 2014-2613*, Atlanta, GA, June 2014.
- ¹⁶Bidwell, C. S. and Potapczuk, M. G., "USERS MANUAL FOR THE NASA LEWIS THREE-DIMENSIONAL ICE ACCRETION CODE (LEWICE 3D)," *NASA TM-1993-105974*, 1993.
- ¹⁷Wilcox, D. C., "Reassessment of the scale-determining equation for advanced turbulence models," *AIAA journal*, Vol. 26, No. 11, 1988, pp. 1299–1310.
- ¹⁸Papadakis, M., Rachman, A., Wong, S.-C., Yeong, H.-W., Hung, K., and Bidwell, C., "Water Impingement Experiments on a NACA 23012 Airfoil with Simulated Glaze Ice Shapes," *AIAA Paper 2004-565*.
- ¹⁹Bidwell, C. S., "Icing Analysis of a Swept NACA 0012 Wing Using LEWICE3D Version 3.48," *6th AIAA Atmospheric and Space Environments Conference, AIAA Paper 2014-2200*, Atlanta, GA, 2014.
- ²⁰Szilder, K. and Lozowski, E., "Progress towards a 3D Numerical Simulation of Ice Accretion on a Swept Wing using the Morphogenetic Approach," Tech. rep., *SAE Paper 2015-01-2162*, June 2015.